Journal of Alloys and Compounds 640 (2015) 193–200

Contents lists available at ScienceDirect

Journal of Alloys and Compounds

journal homepage: www.elsevier.com/locate/jalcom

Magnetic analysis of a melt-spun Fe-dilute $Cu_{60}Au_{35}Fe_5$ alloy

Shin-ichiro Kondo [a,*], Kento Ogawa [a], Takao Morimura [a], Hiromichi Nakashima [a], Shin-Taro Kobayashi [b], Chishiro Michioka [b], Kazuyoshi Yoshimura [b]

[a] Faculty of Engineering, Nagasaki University, 1-14 Bunkyo-machi, Nagasaki 852-8521, Japan
[b] Department of Chemistry, Kyoto University, Kitashirakawa Oiwake-cho, Sakyo-ku, Kyoto 606-8502, Japan

ARTICLE INFO

Article history:
Received 1 December 2014
Received in revised form 31 March 2015
Accepted 2 April 2015
Available online 8 April 2015

Keywords:
Melt-spun
Magnetic measurements
TEM
Cu–Au–Fe
Fe-dilute
Spin glass

ABSTRACT

The magnetic properties of a melt-spun $Cu_{60}Au_{35}Fe_5$ alloy are examined by X-ray diffraction (XRD), magnetic measurements, and transmission electron microscopy (TEM). The XRD pattern of an as-spun sample indicates the formation of a solid solution of Cu and Au with no Fe phase, whereas that of the annealed sample (773 K × 36 ks) shows a small amount of the α-Fe phase because the Fe atoms precipitate during annealing. TEM observations and EDX analysis of the as-spun sample show no distinct Fe-rich domains, implying that some Fe atoms are dissolved in the matrix, and others form very fine magnetic clusters. Moreover, magnetic measurements indicate the presence of magnetic clusters and isolated Fe atoms. The AC magnetic susceptibilities show that the as-spun sample has a sharp cusp around 20 K, which is characteristic of spin glass behavior. The simulations of the *M–H* curves of the as-spun sample measured at 77 and 300 K, show that most Fe atoms are dissolved in the matrix as isolated atoms, not as clusters. Additionally, the calculated rate of clustering in the as-spun sample tends to decrease with temperature, suggesting that the magnetic exchange interactions are weak.

1. Introduction

Fe–Au systems have attracted considerable attention because this system exhibits various magnetic properties such as forming spin glasses, mictomagnetism in Fe-dilute compositions, and ferromagnetism in Fe-rich compositions [1–20]. The measurements of the electrical resistivity of Au–Fe alloys [2] show that spin glasses form in the concentration range of 0.5–8 at.% Fe. When the Fe concentration exceeds about 10 at.%, mictomagnetism appears, which is characterized by large magnetic clusters and a sensitivity to thermal and magnetic history. Further increases in the Fe concentration produce overlapping among the magnetic clusters, finally resulting in the appearance of a long-range inhomogeneous ferromagnetic regime. A magnetic phase diagram [3–5] experimentally obtained by using a number of different techniques suggests that Au–Fe alloys with an Fe composition of less than 15 at.% Fe behave as spin glasses that are characterized by a cusp in the initial susceptibility, whereas the magnetic properties of the alloys with Fe > 15 at.% are similar to those of normal ferromagnets.

The transverse magnetoresistance measured in Au–Fe alloys from 2.9 to 18 at.% Fe [7] shows that the magnetic behavior passes through spin glass, mictomagnetic, and inhomogeneous ferromagnetic regimes as the Fe concentration increases. Hamzić and Campbell concluded from the electrical resistivity and magnetoresistance measurements, that ferromagnetic and spin glass ordering coexist at low temperatures when the composition of Fe exceeds the concentration where ferromagnetic order appears and that the coexistance vanishes and ferromagnetic order appears as the temperature increases [11]. Thus, the magnetic properties of the binary Au–Fe system are complex.

Since the discovery of giant magnetoresistance [21–25], many theoretical and experimental studies have focused on Au–Fe thin films, nanowires, and layered superlattices [26–40]. Ichimura and Sakuma calculated the electronic and magnetic structures of finite-size systems consisting of *n* (=2–12) layers of Au that possess the interface Fe monolayer on one side and the free surface on the other side [30]. They used the linearized muffin-tin orbital method with the atomic sphere approximation within the local spin-density approximation. The magnetic moment of the Fe monolayer changed non-monotonically by 0.1 μ_B as the number of Au layers increased. The finite-temperature properties of the layered Fe/Au superlattice were calculated by Wang et al. [35] by using Monte Carlo simulations based on the Heisenberg model. In the calculations, the exchange parameters were deduced from the ab initio total energies and a phenomenological anisotropy constant was used. The calculated Curie temperature decreased with the decrease in Fe layer thickness, demonstrating that the Curie

* Corresponding author. Tel./fax: +81 95 819 2635.
E-mail address: kondou@nagasaki-u.ac.jp (S.-i. Kondo).

http://dx.doi.org/10.1016/j.jallcom.2015.04.004
0925-8388/

temperature is strongly affected by the ab initio exchange parameters and is insensitive to the anisotropy. Neuttiens et al. examined the experimental behaviors of the differential resistance, $R(I) = dV/dI$, of narrow Au–Fe spin glass wires [32]. They argued that the asymmetric behavior of $R(I)$ could be explained by a mesoscopic thermoelectric effect. Saoudi et al. investigated the size effect in the spin glass magnetization of thin Au–Fe ($Au_{97}Fe_3$) films using polarized neutron reflectometry [38]. Films from 20 to 500 nm thick exhibit Brillouin magnetic behavior at temperatures of 295–50 K with an Fe magnetic moment of 0.9 μ_B below 30 K. However, they reported an Fe magnetic moment of 1.3 μ_B below 20 K for the 10-nm-thick film. Recently, Fritzsche et al. investigated the magnetic properties of ultrathin Au–Fe films [40]. They found that the magnetization of a 1-nm-thick film follows a Brillouin function, showing that ultrathin $Au_{97}Fe_3$ layers less than 1 nm thick are paramagnetic instead of spin glasses.

A melt-spun $Au_{80}Fe_{20}$ alloy was investigated by Allia et al. [41]. The as-quenched melt-spun $Au_{80}Fe_{20}$ alloy exhibited paramagnetic behavior with very short-range magnetic correlations among adjacent spins. Moreover, the melt-spun $Au_{70}Fe_{30}$ alloy exhibited similar magnetic behavior to the $Au_{80}Fe_{20}$ alloy with a higher paramagnetic temperature, T_C (415 K) [42]. The melt-spun $Au_{80}Fe_{20}$ and $Au_{70}Fe_{30}$ alloys both exhibit an isotropic magnetic resistance at room temperature [42].

Au–Fe systems show various magnetic properties that depend on the fabrication method. However, the magnetic properties of most of the ternary alloys, including the Au–Fe system, remain unknown. Therefore, in this study we investigated the melt-spun Cu–Au–Fe alloy, because the phase-diagrams of the Cu–Au–Fe ternary system are interesting. First, equilibrium Au–Fe systems at high temperatures form solid solutions. For example, just below the peritectic temperature of 1446 K, the Au-solid solution and γ-Fe phase coexist with an Au-solid solution containing 74 at.% Fe and γ-Fe containing 8 at.% Au. At 1121 K, up to 47 at.% Fe can be dissolved in an Au solid solution [43]. In the Au–Cu system, all-proportional solid solutions are formed above 683 K. In contrast, Fe and Cu cannot dissolve in each other. The maximum content of Fe in a Cu-based solid solution is 4.8 at.% [44]. Because the solubility of Fe atoms in this ternary alloy system determines the magnetic properties, we expect the system to have various magnetic properties. Furthermore, in this work we use melt quenching apparatus to fabricate the melt-spun sample with a cooling rate of 8×10^5 K/s [45]; thus, we expect the high-temperature phase to be preserved at room temperature. Second, the presence of Au atoms affects the magnetic properties strongly; however, the presence of Cu atoms may prevent Au atoms from coupling magnetically with the Fe atoms because Au–Cu forms an all-proportional solid solution at high temperatures, indicating that the Au–Cu coupling is stronger. As a result, the Cu–Au–Fe ternary systems display interesting magnetic properties.

In this study, we examine the relationship between the magnetization and its characterization using X-ray diffraction (XRD), magnetic measurements, including the AC magnetic susceptibilities, and transmission electron microscopy (TEM) of the melt-spun Cu–Au–Fe alloys. In the Fe-rich melt-spun Cu–Au–Fe alloy, the complicated inter-granular interactions should be considered. Consequently, to discuss the quantitative relationship between the microstructures and magnetic properties, we chose the Fe-dilute Cu–Au–Fe alloy, $Cu_{60}Au_{35}Fe_5$. These Fe-dilute Cu–Au–Fe alloys have never been investigated as magnetic materials. Although Fe-dilute alloys may not be commercially important, they are expected to show interesting magnetic behaviors, such as the formation of spin glasses and mictomagnetism. Our results will elucidate the various unusual magnetic properties observed in Au–Fe alloys fabricated by equilibrium and non-equilibrium methods [1–20,26–42].

2. Sample preparation

Small pieces of oxygen-free Cu (99.99% purity), Au (99.9% purity), and Fe (99.9% purity) were placed in a high-frequency furnace at a weight ratio of Cu–35 at.% Au–5 at.% Fe and were then melted together under argon gas shielding. Melt-spun samples were prepared from specimens fabricated under an argon gas atmosphere using a single roller melt-spinning apparatus. The samples were quenched from liquid at a surface velocity of approximately 42 m/s and a blow-off pressure of 0.6 atm. The melt-spun samples were 50–60 μm thick and 1.0–1.5 mm wide. The samples were sealed in quartz tubes in a vacuum and were aged at 773 K for 36 ks.

XRD with Cu Kα radiation was used to determine the phases formed in the melt-spun and annealed samples at room temperature. The magnetic properties for both samples were measured with an applied field of up to 70 kOe (7 T) at 4.2, 77, and 300 K. The field-cooled (FC) and zero-field-cooled (ZFC) magnetizations were measured in the temperature range of 2–300 K under an applied field of 10 kOe and 50 Oe. The AC magnetic susceptibilities were measured for frequencies between 1 and 997 Hz under an alternating field of 3 Oe. The microstructure was observed by TEM performed on a JEOL JEM2010 high-resolution microscope. The TEM disks (diameter: approx. 3 mm) were punched from the samples and polished by ion milling. Additionally, a beam about 10 nm in diameter was used for EDX composition analysis of small regions.

3. Experiments

3.1. X-ray diffraction

Fig. 1 shows the XRD profiles for as-spun and quenched (hereinafter, As-Q) and annealed (773 K × 36 ks) samples, and for pure Au and Cu. The (111), (200), and (220) reflections of the As-Q and annealed sample are located among the reflections of pure Au and Cu, which indicates the formation of a solid solution. Fig. 2 shows the electron diffraction pattern of the As-Q sample, which has a face-centered cubic (fcc) structure, where the incident direction is [110]. This solid solution phase appears because Au and Cu form an all-proportional solid solution above 683 K and the high-temperature phase can be retained when using melt-spinning apparatus. Additionally, X-ray analysis of $Au_{80}Fe_{20}$ and $Au_{70}Fe_{30}$ melt-spun alloys [46] has shown that the fcc phase is observed even in alloys containing high Fe concentrations, which is consistent with the retention of the high-temperature phase.

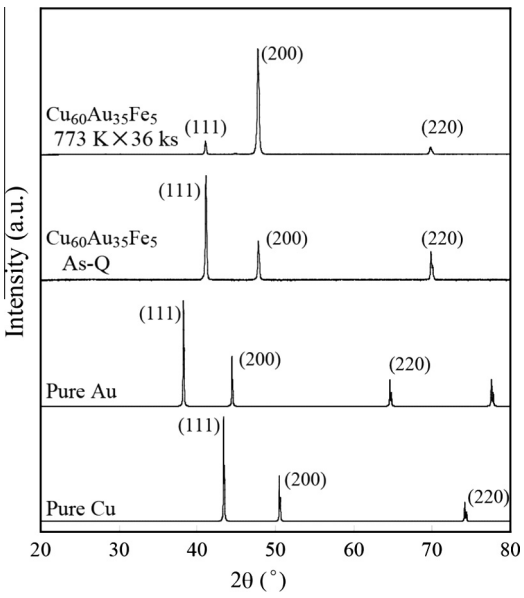

Fig. 1. XRD profiles of the As-Q and annealed (773 K × 36 ks) $Cu_{60}Au_{35}Fe_5$ alloy and of pure Au and Cu.

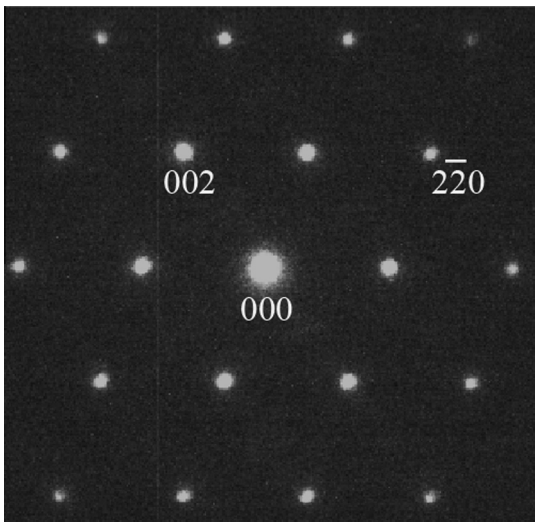

Fig. 2. Electron diffraction pattern of the As-Q sample of the $Cu_{60}Au_{35}Fe_5$ alloy ([1 1 0] incident direction).

Next, we discuss the supersaturation of the As-Q sample in relation to the lattice constant. The lattice constant of the As-Q sample is experimentally determined as 3.794 Å. In contrast, a lattice constant of 3.788 Å is theoretically calculated by applying Vegard's law to the solid solution; thus, the disagreement between the experimental and theoretical results is as small as 0.16%.

A very weak peak is observed around 45° in the XRD profile of the annealed sample (Fig. 1). Fig. 3 shows the magnification of the XRD profiles of the As-Q and annealed samples around 45°. The annealed sample shows the Fe (1 1 0) reflection, whereas the As-Q sample does not, meaning that the Fe atoms are precipitated by annealing. During the Fe precipitation in Cu–Au–Fe alloys [47], fcc γ-Fe segregates with annealing time at temperatures around 683 K. However, our experimental results indicate the segregation of body-centered cubic (bcc) α-Fe. This difference may arise from the differences in composition and annealing temperature; the slight difference in chemical potential caused by the compositional differences may have a large effect on the precipitation mechanism. Additionally, the absence of the Fe (1 1 0) reflection in the As-Q sample suggests that the Fe atoms form very fine clusters or are isolated in the matrix.

3.2. Magnetic measurements

Fig. 4 shows the magnetization curves (*M*–*H* curves) of the As-Q and annealed samples at 300 K. The magnetization of the annealed sample is almost saturated at more than 20 kOe, whereas that of the As-Q sample is very small and unsaturated as it increases linearly.

The residual magnetization is 2 emu/g for the annealed sample, whereas no residual magnetization is observed in the As-Q sample. The 1/*H* plot shows that the saturated magnetization of the annealed sample is 5.8 emu/g. The magnetization of $Cu_{60}Au_{35}Fe_5$ is 5.6 emu/g, assuming that the Fe atoms couple ferromagnetically with a magnetic moment of 2.2 μ_B. The magnetic measurements and the XRD

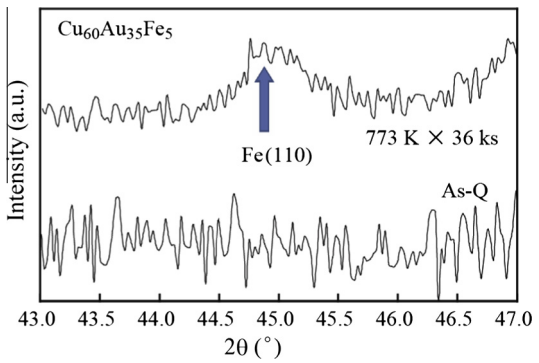

Fig. 3. Magnification of the XRD profile of the As-Q and annealed $Cu_{60}Ag_{35}Fe_5$ alloy between 43.0° and 47.0°.

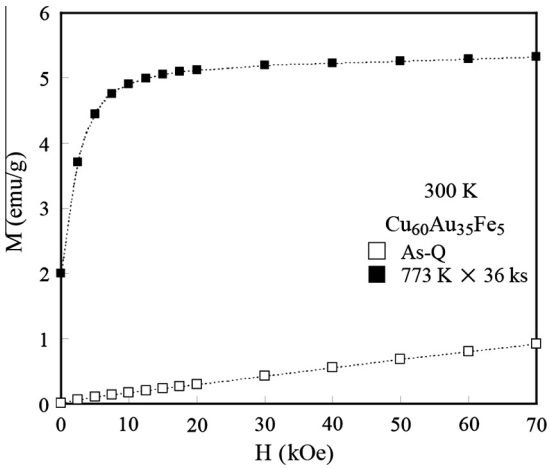

Fig. 4. *M*–*H* curves for the As-Q and annealed $Cu_{60}Ag_{35}Fe_5$ alloy measured at 300 K. □: As-Q; ■: annealed (773 K × 36 ks).

results show that the magnetization of the annealed sample is that of bcc α-Fe. Furthermore, the precipitation of antiferromagnetic fcc γ-Fe [47] is not observed in this sample.

Fig. 5 shows the *M*–*H* curves of the As-Q and annealed samples at 77 K. Compared with the curves at 300 K, the magnetization of the As-Q sample increased, although that of the annealed sample showed only a slight increase.

Fig. 6(A) and (B) shows the *M*–*H* curves of the As-Q and annealed samples measured at 4.2 K. Both samples show hysteresis curves, with a coercive force of 500 Oe for the As-Q sample and 1 kOe for the annealed sample. The magnetization of the annealed sample reaches saturation, whereas that of the As-Q sample is not saturated, even at 4.2 K under an applied field of 70 kOe.

Compared with the results in Figs. 4–6, the magnetic behavior of the annealed sample does not change dramatically with the decrease in temperature, which can be explained by the precipitation of the α-Fe phase by annealing. The magnetic behavior of the As-Q sample is completely different from that of the annealed sample. The As-Q sample is very sensitive to the temperature; it has a small, unsaturated magnetization even at 4.2 K under an applied field of 70 kOe.

The magnetization temperature dependences (*M*–*T* curves) for the As-Q and annealed samples, both of which show FC magnetization, are measured in the temperature range of 4.2–300 K under an applied field of 10 kOe (Fig. 7). There are large differences in the magnetic behavior of the samples. The As-Q sample shows a strong temperature dependence, whereas the magnetization of the annealed sample remains almost constant over the whole temperature range, confirming the effect of Fe. The change in magnetization is steep in the As-Q sample; the magnetization at 300 K is one-tenth that at 4.2 K. The rate of the decrease in magnetization is large between 30 and 80 K.

Fig. 8 shows the FC and ZFC magnetizations of the As-Q sample under an applied field of 50 Oe in the temperature range of 2–100 K, with a distinct cusp around $T_p \approx 19.8$ K for ZFC magnetization. The irreversibility between FC and ZFC processes, namely bifurcation at a temperature of less than T_p, implies the presence of magnetic metastable states, which are widely found in various magnetic

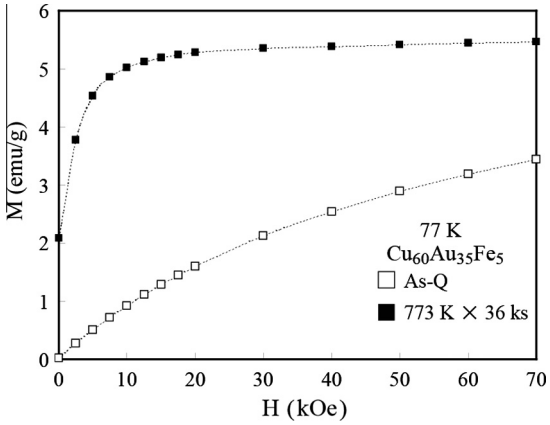

Fig. 5. *M*–*H* curves for the As-Q and annealed $Cu_{60}Ag_{35}Fe_5$ alloy measured at 77 K. □: As-Q; ■: annealed (773 K × 36 ks).

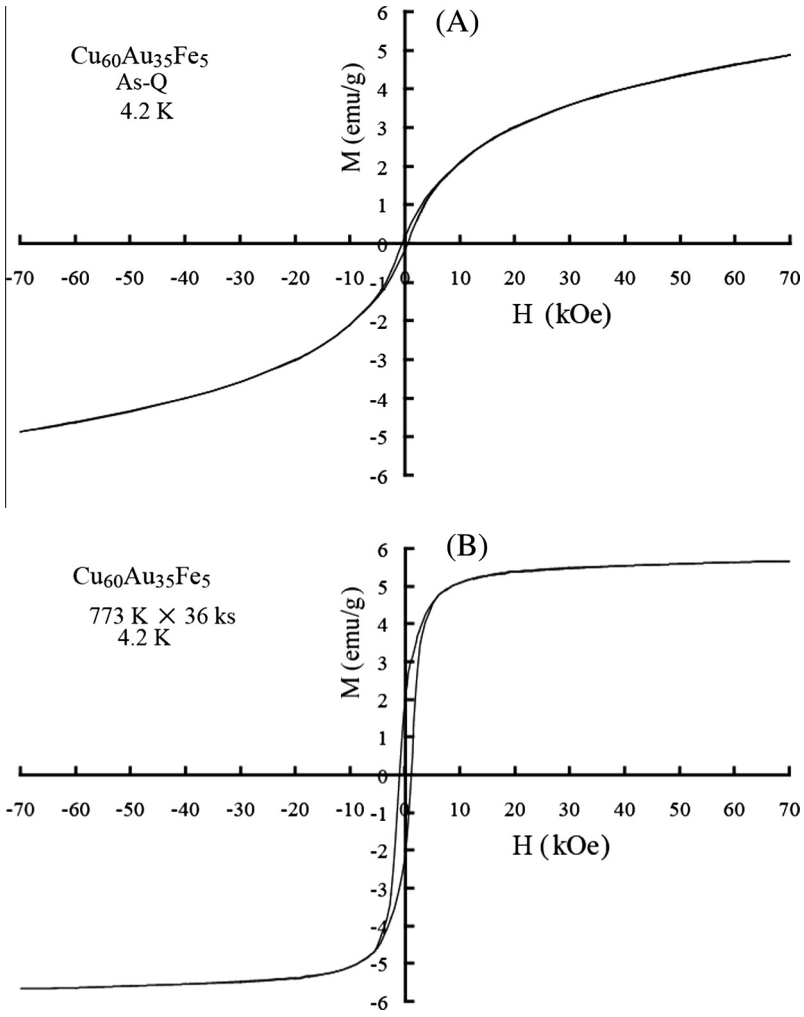

Fig. 6. *M–H* curves for the (A) As-Q and (B) annealed (773 K × 36 ks) $Cu_{60}Ag_{35}Fe_5$ alloy measured at 4.2 K.

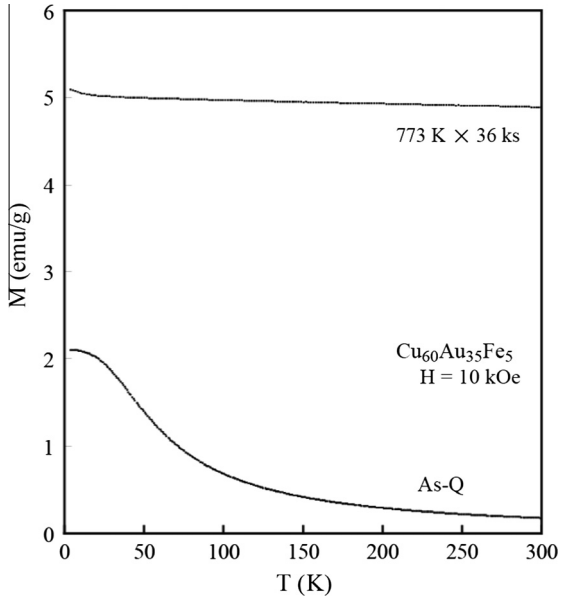

Fig. 7. *M–T* curves for the As-Q and annealed $Cu_{60}Ag_{35}Fe_5$ alloy measured under an applied field of 10 kOe.

materials, such as spin glasses, cluster glasses, mictomagnets, and superparamagnets. Although each metastable state in these materials has physically different meanings, it is usually caused by the effect of the random local anisotropy field on the appearance of bifurcation. Here, the bifurcation is caused by the presence of random local anisotropy field; therefore, the magnetic field of 50 Oe is sufficiently weak in comparison. Accordingly, the small coercive force of 500 Oe was probably caused by the random local anisotropy field (Fig. 6(A)).

The inverse magnetic susceptibility ($1/\chi$) versus temperature (T) plots for $T > 20$ K, which is evaluated from FC magnetization in the As-Q sample, are shown in Fig. 9, following the Curie law. When the applied field is very weak, $1/\chi$ is

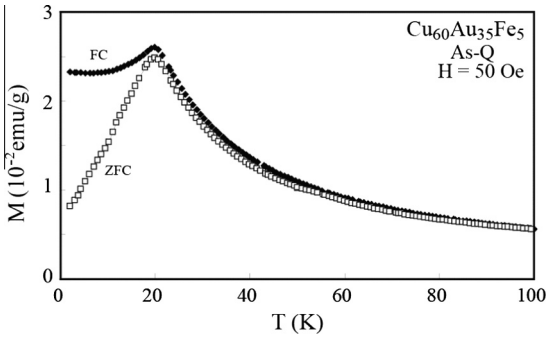

Fig. 8. FC and ZFC magnetizations of the As-Q sample under an applied field of 50 Oe in the temperature range 2 to 100 K. ◆: FC magnetization; □: ZFC magnetization.

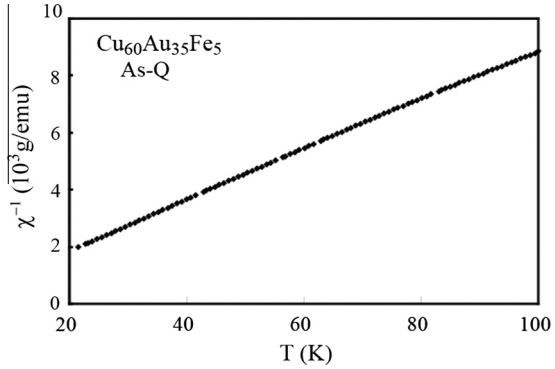

Fig. 9. Plots of inverse magnetic susceptibility $1/\chi$ versus temperature T at $T > 20$ K, evaluated from FC magnetization in the As-Q sample.

$$\frac{1}{\chi} = \frac{3k_B}{N_0 m_0^2} T \tag{1}$$

Here, N_0 is the number of Fe atoms, m_0 is the effective magnetic moment of the atom and k_B is the Boltzmann coefficient. From Eq. (1) we obtain the value of $m_0 \approx 14.1\ \mu_B$, suggesting partial formation of some very small clusters in the matrix.

Fig. 10 shows the temperature dependence of the real part of the AC magnetic susceptibilities, χ', for the As-Q sample at a frequency of 997 Hz with an applied field of 3 Oe. A sharp cusp at $T = 20.6$ K, which is characteristic of spin glass, is observed.

Fig. 11 shows the detailed temperature dependences of χ' for the As-Q sample at seven frequencies from 1 to 997 Hz around the cusp. The spin glass freezing temperature, T_g, which is the temperature where the cusp appears, shifts toward a higher temperatures as the frequency increases. The relative variation in T_g per decade of frequency, ω, expressed as $\Delta T_g/[T_g \cdot \Delta(\log_{10}\omega)]$, is about 1.5×10^{-2}. This value is small compared with the value of 4×10^{-2} for the cluster spin glass $SrFe_{0.9}Ti_{0.1}O_{3-\Delta}$ [48], and it is larger than that of the classical spin glass of the CuMn alloy (5×10^{-3}) and other canonical spin glasses [49].

Based on the dynamical scaling approaches [48,50-56], each measurement time, τ, is expressed as

$$\tau = \tau_0 \left(\frac{T_g(\omega) - T_0}{T_0} \right)^{-zv} \tag{2}$$

where τ_0 is the microscopic flipping time, z is the dynamic exponent, and v is the spin correlation exponent. $T_g(\omega)$ and T_0 denote the spin glass freezing temperature at frequency ω and $\omega \to 0$, respectively. The best fitting results based on Eq. (2) are shown in the inset of Fig. 11. The optimized values of zv and T_0 are 10.3 and 18.7 K, respectively. zv for conventional spin glass systems ranges from 7 to 11 [48,51–53,56]; therefore, the optimized value of $zv = 10.3$ is a typical value for conventional spin glass.

3.3. TEM observations and EDX analysis

Fig. 12 shows the bright-field TEM image of the As-Q sample. Banded structures are visible, although the grain size is not clear. Therefore, the precise grain size cannot be determined. Fig. 12(A) shows a precipitate, indicated with circles labeled 1–4

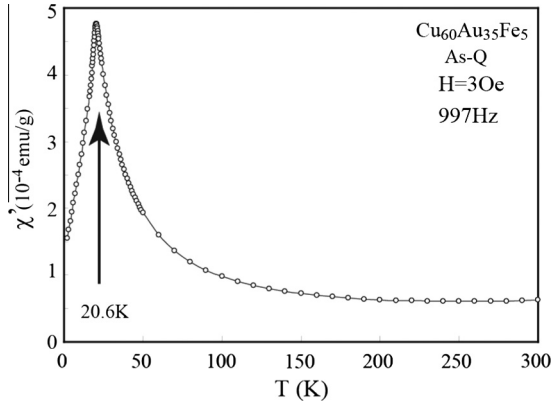

Fig. 10. Temperature dependence of the real part of the AC magnetic susceptibilities, χ', for the As-Q sample at a frequency of 997 Hz with an applied field of 3 Oe.

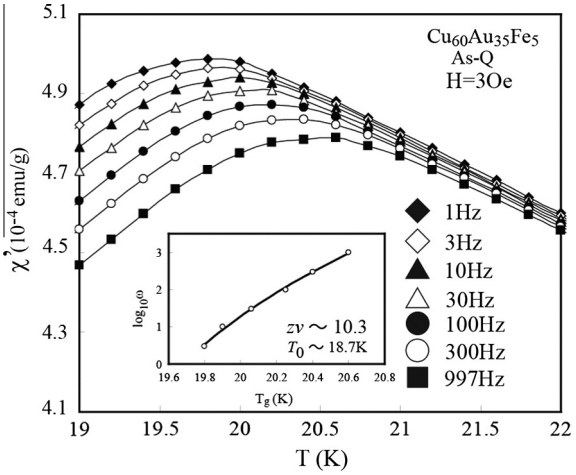

Fig. 11. Detailed temperature dependences of χ' for the As-Q sample at seven frequencies from 1 to 997 Hz around the cusp. Inset: best fit results with Eq. (2).

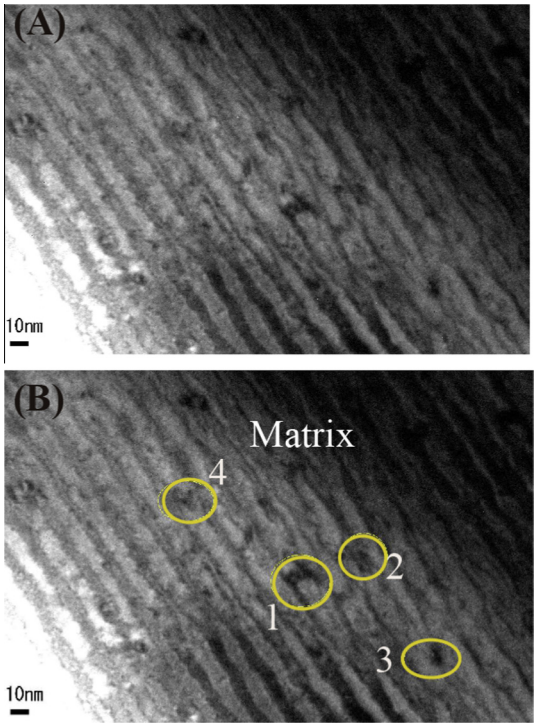

Fig. 12. (A) TEM bright-field micrograph of the As-Q $Cu_{60}Au_{35}Fe_5$ alloy. (B) Total image with areas 1–4 containing precipitates marked with circles.

(areas 1–4) in Fig. 12(B). Additionally, the matrix is defined as the material that surrounds these precipitates. Table 1 shows the EDX analysis for area 1 (Fig. 12(B)) and

Table 1
EDX analysis results for the matrix and area 1.

Element	at.%
Matrix	
Fe	5.2
Cu	63.9
Au	30.9
Area 1	
Fe	6.6
Cu	64.7
Au	28.7

the matrix. There are no clear compositional differences between the precipitate and matrix. For example, the Fe content is 5.2 at.% in the matrix area, whereas it is 6.6 at.% in area 1; a difference of only 1.4 at.%.

If the magnetism originates from the magnetic precipitates in areas 1–4, then the Fe content in area 1 should be higher than 6 at.%. However, EDX analysis suggests that there are no Fe-rich areas, although there are slight compositional differences between the precipitate and matrix. Additionally, as shown in Fig. 2, only a complete fcc solid solution is observed with no other ordered magnetic phases or precipitates. Thus, areas 1–4 in Fig. 12(B) are not magnetic precipitates and are other structures presumably introduced into matrix when the sample is rapidly quenched. The size of the magnetic clusters may be too small to be detected by TEM or may be dissolved in the matrix as isolated atoms.

Fig. 13 shows the bright-field TEM image of the annealed sample (773 K for 36 ks). The XRD and magnetic analysis suggest Fe precipitation in the matrix, and Fig. 13(A) shows needle-like precipitates of about 100 nm in length. Compositional analysis was performed on Area 1 in Fig. 13(A) to determine whether the precipitates were Fe. Fig. 13(B) is the magnification of Area 1, including the EDX2 region in the matrix and the EDX5 region in the precipitate.

The EDX spectra for the EDX2 and EDX5 regions are shown in Fig. 14. Fig. 14(A) contains only Cu and Au peaks, and no Fe peaks are observed in the EDX2 matrix region, indicating there were no Fe atoms in the matrix. However, Fig. 14(B) shows that the EDX5 area of the needle-like precipitate contained Fe Kα and Fe Kβ peaks. Cu and Au peaks are also detected in this area because of the large diameter of a beam (7 nm). These results indicate that the needle-like precipitates are mainly Fe atoms. The EDX analysis of the annealed sample and the As-Q sample demonstrate that annealing at 773 K for 36 ks dissolves the Fe atoms homogeneously in the matrix to form large Fe precipitates, leaving almost no Fe atoms in the matrix.

4. Analysis

As shown in Figs. 4 and 5, the M–H curves of the As-Q sample measured at 300 and 77 K show superparamagnetic and paramagnetic behaviors with no coercive force or residual magnetization because the measured temperatures of 300 and 77 K are much higher than the spin glass freezing temperature, T_g. The magnetic behavior of the annealed sample is caused by the Fe

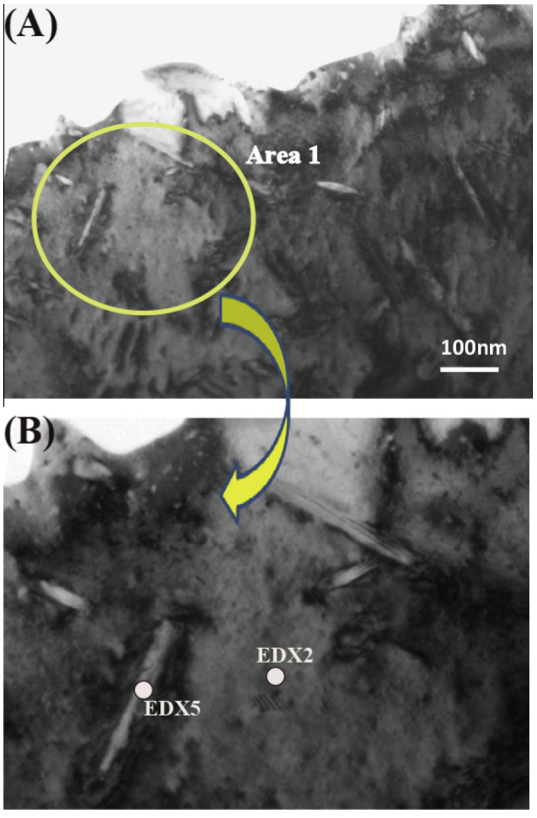

Fig. 13. (A) Whole image of the bright-field TEM for the annealed sample (773 K for 36 ks). (B) Magnification of Area 1. EDX2 and EDX5 are the areas used for the compositional analysis.

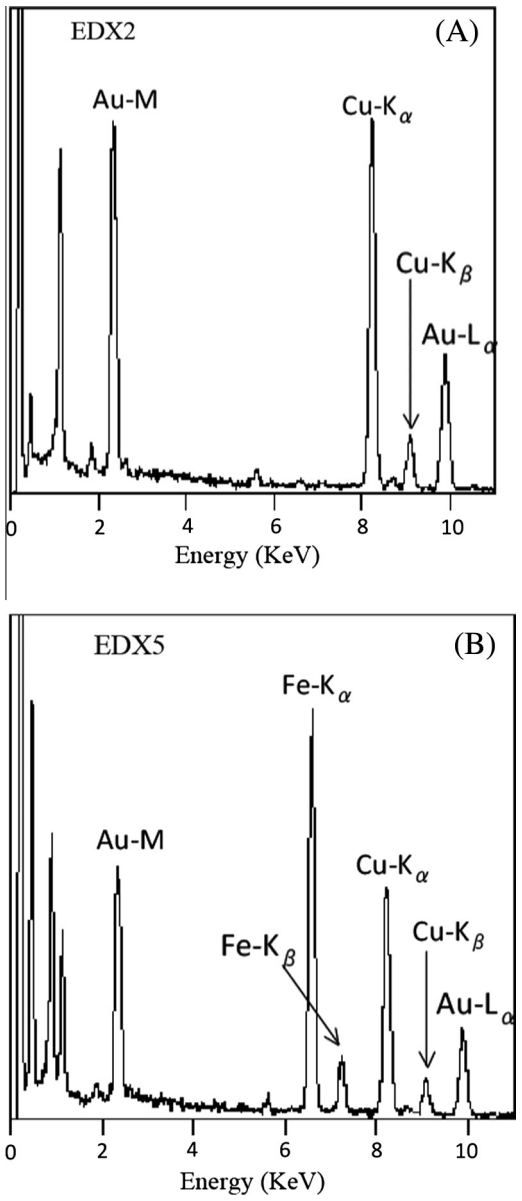

Fig. 14. (A) EDX spectrum for area EDX2. No peaks associated with Fe are observed. (B) EDX spectrum for area EDX5. Fe Kα and Fe Kβ peaks are observed.

precipitates and phase; therefore, we focus on the magnetic properties of the As-Q sample by analyzing the M–H curves.

The estimated value of the effective magnetic moment of $m_0 \approx 14.1\ \mu_B$ per Fe atom indicates that most Fe atoms are partially dissolved as isolated atoms or are partially aggregated as small fine clusters. Therefore, it is important to determine the fraction of Fe atoms present as clusters to clarify whether Fe atoms are present as matrix clusters or as isolated atoms.

Next, we analyze the M–H curves of the As-Q sample by using the method proposed by Saoudi et al. [39], focusing on evaluating the fraction of clusters, f.

First, we define $m_{obs}(H)$ as the observed magnetic moment per Fe atom, and $m_{obs}(H)$ satisfies

$$m_{obs}(H) = f m_{cl}(H) + (1-f) m_{is}(H) \tag{3}$$

$$m_{cl}(H) = g\mu_B J_{cl} B\left(n_{cl} J_{cl}, \frac{g n_{cl} J_{cl} \mu_B H}{k_B T}\right) \tag{4}$$

$$m_{is}(H) = g\mu_B J_{is} B\left(J_{is}, \frac{gJ_{is}\mu_B H}{k_B T}\right) \quad (5)$$

In Eqs. (3)–(5), $m_{cl}(H)$ and $m_{is}(H)$ are the calculated magnetic moment per Fe atom associated with the clusters and isolated atoms, respectively. g is the gyromagnetic ratio ($g = 2$) and n is the number of Fe atoms per cluster ($n = 60$). $B(J, x)$ denotes the Brillouin function with the total angular moment, J, defined as

$$B(J,x) \equiv \frac{2J+1}{2J}\coth\left[\frac{2J+1}{2J}x\right] - \frac{1}{2J}\coth\left[\frac{1}{2J}x\right]$$
$$x = \frac{gJ\mu_B H}{k_B T} \quad (6)$$

Fitting results are displayed in Fig. 15. The experimental and theoretical data agree well, and the optimized total angular moments for cluster and isolated atoms, J_{cl} and J_{is}, are 3/2 and 3, respectively. The value of f at 300 K is 0.064 (6.4%), whereas that at 77 K is 0.201 (20.1%), indicating that most Fe atoms are dissolved in the matrix as isolated atoms and that the rate of clustering decreases with temperature. This decrease is presumably caused by weak magnetic exchange interactions between Fe atoms; 300 K is a sufficiently high temperature to destroy magnetic bonding. In addition, the unsaturated magnetization at 4.2 K under an applied field of 70 kOe probably caused by the presence of isolated Fe atoms in the matrix (Fig. 6(A)).

5. Conclusion

We have examined the magnetic properties of a melt-spun Fe-dilute $Cu_{60}Au_{35}Fe_5$ alloy using XRD, magnetic measurements, and TEM. The XRD profiles of the As-Q sample show the formation of a solid solution. In the electron diffraction pattern of the As-Q sample, the crystalline structure of the solid solution is fcc and there is no bcc structure. The TEM images and EDX analysis showed no distinct magnetic particles or Fe-rich domains in the As-Q sample; there was a compositional difference of only about 1 at.%, indicating there were no iron rich domains. Because Cu and Au form an all-proportional solid solution above about 700 K, most Fe atoms are dissolved in the matrix with some atoms partially forming fine magnetic clusters, neither of which can be detected by TEM.

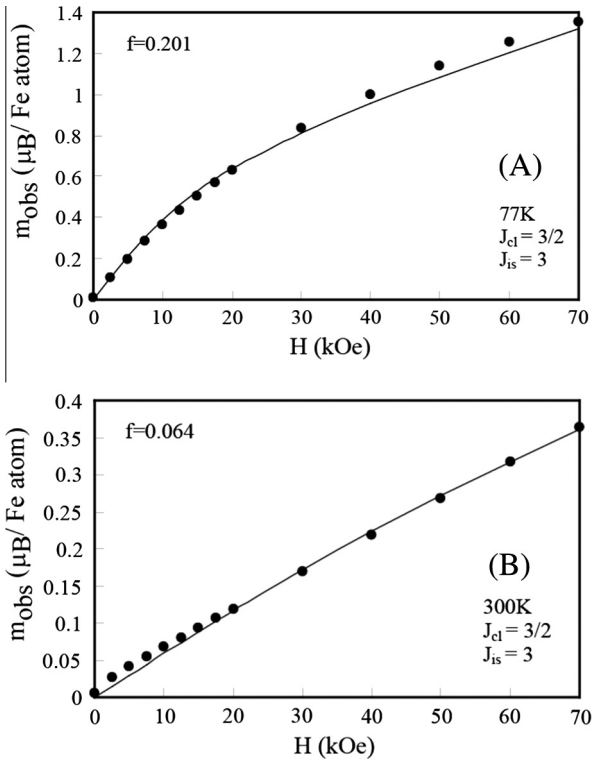

Fig. 15. Fitting results for the 77 and 300 K M–H curves based on Eqs. (3)–(5). ●: experimental data; solid line: theoretically estimated curves.

In contrast, the Fe (1 1 0) reflection is observed in the XRD profiles of the annealed sample (773 K × 36 ks) owing to Fe precipitation caused by annealing. The TEM images revealed needle-like precipitates about 100 nm in length in the matrix. The EDX analysis showed that the precipitates were composed of Fe. Furthermore, the saturated magnetization of the annealed sample indicated the precipitation of Fe atoms.

Next, we examined the magnetic properties, focusing on the As-Q sample. The real part of the AC magnetic susceptibilities, χ', for the As-Q sample contained a sharp cusp at around $T \approx 20$ K, indicating that a spin glass appears at temperatures below the spin glass freezing temperature, T_g.

For temperatures above T_g, we evaluated the effective magnetic moment per Fe atom as about 14.1 μ_B from the inverse magnetic susceptibility, $1/\chi$, versus T plots. The results showed that in the As-Q sample, some Fe atoms were partially dissolved in the matrix and some formed very fine magnetic clusters. This is consistent with the TEM and EDX analysis. Therefore, the M–H curves of the As-Q sample show superparamagnetic and paramagnetic behaviors at $T > T_g$

To determine the rate of magnetic clustering, f, we applied the magnetic analysis proposed by Saoudi et al. [39] to the M–H curves at 77 and 300 K. The results showed that most Fe atoms were dissolved in the matrix as isolated atoms. In addition, f decreased with temperature, implying that the magnetic exchanges between Fe atoms are weak.

References

[1] V. Cannella, J.A. Mydosh, Phys. Rev. B 6 (1972) 4220.
[2] J.A. Mydosh, P.J. Ford, M.P. Kawatra, T.E. Whall, Phys. Rev. B 10 (1974) 2845.
[3] A.P. Murani, S. Roth, P. Radhakrishna, B.D. Rainford, B.R. Coles, K. Ibel, G. Goeltz, F. Mezel, J. Phys. F6 (1976) 425.
[4] B.H. Veerbeck, J.A. Mydosh, J. Phys. F8 (1978) L–111.
[5] B.R. Coles, B.V.B. Sarkissian, R.H. Taylor, Philos. Mag. B 37 (1978) 489.
[6] S.P. McAlister, J. Phys. Colloques 39 (1978). C6-893.
[7] A.K. Nigam, A.K. Majumdar, J. Appl. Phys. 50 (1979) 1712.
[8] J.J. Smit, G.J. Nieuwenhuys, L.J. de Jongh, Solid State Commun. 32 (1979) 233.
[9] S. Senoussi, J. Phys. Lett. 41 (1980) 571.
[10] S. Senoussi, J. Phys. F: Met. Phys. 10 (1980) 2491.
[11] A. Hamzić, I.A. Campbell, J. Phys. Lett. 42 (1981) L–309.
[12] J. Lauer, W. Keune, Phys. Rev. Lett. 48 (1982) 1850.
[13] I.A. Campbell, S. Senoussi, F. Varret, J. Teillet, A. Hamzić, Phys. Rev. Lett. 50 (1983) 1615.
[14] J. Van Cauteren, L. Hermans, J. Appl. Phys. 55 (1984) 1732.
[15] Y. Nakai, Y. Furukawa, N. Kunitomi, J. Magn. Magn. Mater. 54–57 (1986) 155.
[16] Kh. Ziq, J.S. Kouvel, J. Appl. Phys. 63 (1988) 4346.
[17] Y. Furukawa, Y. Nakai, N. Kunitomi, J. Phys. Soc. Jpn. 59 (1990) 2237.
[18] Chen-Chia Chou, C.M. Wayman, J. Mater. Res. 7 (1992) 321.
[19] Y. Furukawa, Y. Nakai, N. Kunitomi, J. Phys. Soc. Jpn. 62 (1993) 306.
[20] S. Radha, A.K. Nigam, G. Chandra, J. Phys.: Condens. Matter 6 (1994) 4945.
[21] J. Wecker, R. von Helmholt, L. Schultz, K. Samwer, Appl. Phys. Lett. 62 (1985) 1993.
[22] A.E. Berkowitz, J.R. Mitchell, M.R. Carey, A.P. Young, S. Zhang, F.E. Spada, F.T. Parker, A. Hutten, G. Thomas, Phys. Rev. Lett. 68 (1992) 3745.
[23] J.Q. Xiao, J.S. Jiang, C.L. Chien, Phys. Rev. Lett. 68 (1992) 3749.
[24] B. Dieny, A. Chamberod, C. Cowache, J.B. Genin, S.R. Teixeira, R. Ferr, B. Barbara, J. Magn. Magn. Mater. 135 (1994) 191.
[25] F. Conde, C. Gómez-Polo, A. Hernando, J. Magn. Magn. Mater. 138 (1994) 123.
[26] K. Koike, T. Furukawa, G.P. Cameron, Y. Murayama, Phys. Rev. B 50 (1994) 4816.
[27] Y. Murayama, K. Koike, J. Magn. Magn. Mater. 140–144 (1995) 659.
[28] K. Takanashi, S. Mitani, M. Sano, H. Fujimori, H. Nakajima, A. Osawa, Appl. Phys. Lett. 67 (1995) 1016.
[29] K. Takanashi, S. Mitani, K. Himi, H. Fujimori, Appl. Phys. Lett. 72 (1998) 737.
[30] M. Ichimura, A. Sakuma, J. Magn. Magn. Mater. 177–181 (1998) 1311.
[31] J-T. Wang, Z-Q. Li, Q. Sun, Y. Kawazoe, J. Magn. Magn. Mater. 183 (1998) 42.
[32] G. Neuttiens, J. Eom, C. Strunk, H. Pattyn, C. Van Haesendonck, Y. Bruynseraede, V. Chandrasekhar, Europhys. Lett. 42 (1998) 185.
[33] J-T. Wang, Z-Q. Li, L. Zhou, Y. Kawazoe, D.-S. Wang, Phys. Rev. B 59 (1999) 6974.

[34] J.-T. Wang, L. Zhou, Y. Kawazoe, D.-S. Wang, Phys. Rev. B 60 (1999) 3025.
[35] J.-T. Wang, L. Zhou, D.-S. Wang, Y. Kawazoe, J. Magn. Magn. Mater. 226–230 (2001) 633.
[36] H. Fritzsche, J. Root, K. Temst, C. Van Haesendonck, Physica B 385–386 (2006) 378.
[37] H. Fritzsche, M. Saoudi, K. Temst, C. Van Haesendonck, Physica B 397 (2007) 47.
[38] M. Saoudi, H. Fritzsche, G.J. Nieuwenhuys, M.B.S. Hesselberth, Phys. Rev. Lett. 100 (2008) 057204.
[39] M. Saoudi, K. Temst, C. Van Haesendonck, M.R. Fitzsimmons, H. Fritzsche, J. Phys: Conf. Ser. 200 (2010) 032063.
[40] H. Fritzsche, J.M. van der Knaap, M.B.S. Hesselberth, G.J. Nieuwenhuys, Phys. Rev. B 81 (2010) 132402.
[41] P. Allia, M. Coisson, V. Selvaggini, P. Tiberto, F. Vinai, Phys. Rev. B 63 (2001) 180404.
[42] P. Allia, M. Coisson, J. Moya, V. Selvaggini, P. Tiberto, F. Vinai, Phys. Status Solidi (a) 189 (2002) 321.
[43] H. Okamoto, T.B. Massalski, L.J. Swartzendruber, P.A. Beck, Bull. Alloys Phase Diagrams 5 (1984) 592.
[44] O. Kubaschewski, Iron-Binary Phase Diagrams, Springer-Verlag, 1982, pp. 35–37.
[45] H. Miyake, A. Furusawa, T. Ariyasu, A. Okada, Imono 66 (1994) 734.
[46] E. Bosco, S. Enzo, M. Baricco, J. Magn. Magn. Mater. 262 (2003) 136.
[47] D.K-H. Finkler, T. Heck, A.E. Maurer, S.J. Campbell, U. Gonser, J. Mater. Sci. 23 (1988) 3480.
[48] A. Sendil Kumar, P.D. Babu, S. Srinath, Mater. Res. Bull. 51 (2014) 332.
[49] J.A. Mydosh, Spin Glasses: An Experimental Introduction, Taylor and Francis, London, 1993. p. 67.
[50] A.T. Ogielski, I. Margenstern, Phys. Rev. Lett. 54 (1985) 928.
[51] A.T. Ogielski, Phys. Rev. B 32 (1985) 7384.
[52] Y. Zhou, C. Rigaux, A. Mycielski, M. Menant, N. Bontemps, Phys. Rev. B 40 (1989) 8111.
[53] B. Martínez, A. Labarta, R. Rodríguez-Solá, X. Obradors, Phys. Rev. B 50 (1994) 15779.
[54] K. De, M. Patra, S. Majumdar, S. Giri, J. Phys. D 40 (2007) 7614.
[55] M. Thakur, M. Patra, S. Majumdar, S. Giri, J. Appl. Phys. 105 (2009) 073905.
[56] Q.Y. Dong, B.G. Shen, J. Chen, J. Shen, J.R. Sun, Solid State Commun. 151 (2011) 12.